Engineering Fracture Mechanics 281 (2023) 109060

Contents lists available at ScienceDirect

Engineering Fracture Mechanics

journal homepage: www.elsevier.com/locate/engfracmech

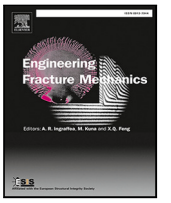

On enrichment strategies and methods to extract stress intensity factors using extended finite element method for bimaterials

Min Ru [a,b], Chuanqi Liu [a,*,1], Yujie Wei [a,b,**,2]

[a] State Key Laboratory of Nonlinear Mechanics, Institute of Mechanics, Chinese Academy of Sciences, Beijing, 100190, China
[b] School of Future Technology, University of Chinese Academy of Sciences, Beijing 100049, China

ARTICLE INFO

Keywords:
X-FEM
Bimaterial
Enriching scheme
Stress intensity factor

ABSTRACT

The eXtended Finite Element Method (X-FEM) is a versatile tool to model cracks and interfaces where sharp gradients and even discontinuity of deformation across the interface may occur. The enrichment functions are introduced to depict possible discontinuity and singularity known from analytical solutions. For bimaterials, the gradients of the displacements are discontinuous across the interface, which can be modeled by ramp functions. In this work, we check the role of the enrichment strategies with and without ramp functions for the accuracy of enriching schemes, and also compare three different methods, i.e. the Interaction Integral Method (IIM), Contour Integration Method (CIM), and Displacement Correlation Method (DCM), to extract the Stress Intensity Factors (SIFs). Both planar and non-planar examples are employed to examine the enriching strategies and the three SIF extraction methods. We find that the enriched ramp functions can improve the accuracy in terms of strain energy, but do not significantly affect the SIFs. The IIM is the best choice to extract SIFs and the DCM can provide enough accuracy with a careful choice of extraction parameters. This work can help a reader when choose the enriching strategies and the extraction methods of the SIFs for interface cracks between dissimilar materials.

1. Introduction

With the increasing demands on multi-functional needs in mechanical, aerospace and biomedical applications, the development of multi-layered material systems has come to the forefront. The overall mechanical behaviors and responses of layered systems hinge on the mechanical properties and fracture behaviors of the interfaces. The interface crack therefore is one of the most commonly encountered failure modes in composites and can cause severe safety problems.

Numerical models of the interface crack are significant to understand and describe the behaviors of the bimaterials. The Finite Element Method (FEM), as one of the most widely used numerical techniques, requires very fine meshes conforming to the interface boundary to obtain acceptable results [1,2]. The singularity of the displacement field should be carefully considered, such as using singular elements [3–5]. Alternatively, the X-FEM [6–8] incorporates additional functions into the standard polynomial space on the basis of partition of unity method [9]. The crack thus can be independent with the meshes of the physical domain.

In terms of the angle between crack and the interface, the X-FEM was first implemented to the scenario that the crack is perpendicular to the material interface [10]. When cracks lie along the material interfaces, Sukumar et al. [11] proposed the

* Corresponding author.
** Corresponding author at: State Key Laboratory of Nonlinear Mechanics, Institute of Mechanics, Chinese Academy of Sciences, Beijing, 100190, China.
E-mail addresses: chuanqil@imech.ac.cn (C. Liu), yujie_wei@lnm.imech.ac.cn (Y. Wei).
[1] Associate Professor.
[2] Professor.

https://doi.org/10.1016/j.engfracmech.2023.109060
Received 17 October 2022; Received in revised form 4 January 2023; Accepted 6 January 2023
Available online 18 January 2023

enrichment functions considering the analytical solution of the displacement field and these enrichment functions were also used by Huynh and Belytschko [12],Jung et al. [13],Yu et al. [14],Dimitri et al. [15]. When a crack terminates at the material interface with arbitrary angles, Bouhala et al. [16] proposed various enrichment functions for different crack angles. Since most cracks propagate along the interface, we here only consider the situation that the crack lies along the material interface. There are two features for this situation, i.e. the jump and singularity of the displacement caused by the crack, and the strain discontinuity (discontinuous spatial gradients of displacement) caused by the material interface. Since we can attain the analytical solution of the displacement for the case that the crack locates at the interface of the bimaterial, the enrichment functions can be directly derived according to the solution [15,17,18]. Moreover, the weak discontinuities can be modeled by signed distance functions with discontinuous gradients and incorporated into the enrichment schemes [12,19]. We here first aim to compare these two enrichment strategies (with or without signed distance functions) in terms of the convergence rate and accuracy.

Though there are many criteria to determine the fracture strength and deflection [20–22], the Stress Intensity Factors (SIFs) of interface cracks are the most widely-used indicators for the fracture mechanics. It is therefore paramount to obtain accurate estimations of SIFs in order to evaluate the overall structural responses and design reliable layered structures. Contrary to homogeneous materials, bimaterial interface cracks always induce both opening and shear deformations even under pure mode loading [23]. Furthermore, the near-tip displacement and singular stress fields of interface cracks are oscillatory, which can be characterized by a complex-valued SIF $\mathrm{K} = K_I + \mathrm{i}K_{II}$ [24]. The real numbers K_I and K_{II} denote the Mode I and II SIFs, respectively. While some analytical solutions for the complex SIF are available in the literature [24,25], they are invariably limited to simple geometries and loading conditions due to inherent mathematical complexities. Various numerical methods have been suggested to evaluate the complex SIFs of interface cracks. These methods can be grouped into direct approaches that correlate the numerical results of near-tip displacements or stresses with analytical solutions [26,27] and energy approaches which are based on energetic quantities like Strain Energy Release Rates (SERRs).

The Displacement Correlation Method (DCM) is one of the simplest direct approaches to extract SIFs [28–30]. While the DCM is a straightforward method for SIF extraction since it involves sampling data computed behind the crack tip only, it requires a high-fidelity displacement field to return accurate and robust results. Some improvements have been proposed to compute highly accurate SIFs using the DCM [31–33]. The most well-known energy approaches used for interface cracks include the Interaction Integral Method (IIM) [34–37] which is an extended version of the J-integral [38] or its domain variant [39], the Contour Integral Method (CIM) based on the Betti's law [40,41]. While additional post-processing steps are often required by energy methods, in general they do yield more accurate and robust results than the direct correlation methods [18]. Within the X-FEM context, the IIM has been predominately used for the SIFs estimation of interface cracks due to its high accuracy and excellent convergence property [12,19,37,42]. In order to obtain the individual modes of SIFs, this method relies on the proper definition of auxiliary solutions and is sensitive to the accuracy of the selected auxiliary fields. The CIM is a superconvergent technique for the extraction of SIFs proposed by Szabo and Babuška [41]. This method is based on the computation of functionals from numerical solutions and the so-called extraction functions. The extraction functions are developed for isotropic materials [43–45] and for bimaterials [46,47]. It is a superconvergent technique since the computed quantities converge to their true values at least as fast as the strain energy. We here second aim to compare these three extraction schemes of SIFs (DCM, IIM and CIM) in terms of the accuracy.

In this work, we focus on the case that the crack lies along the material interface. Various enrichment schemes and extraction methods for the SIFs are quantitatively compared to find the most efficient and accurate schemes within the framework of the X-FEM. The paper is organized as follows. Section 2 describes the problem setting, enrichment schemes for the X-FEM and special treatment to curve cracks. Section 3 presents the different extraction methods of the SIFs. Section 4 demonstrates the results. Section 5 concludes the paper with remarking conclusions.

2. Problem setting and displacement approximation

In this section, we first review the analytical solution of displacement near the crack tip of bimaterials for completeness, and then give two approximations of displacement in the X-FEM.

2.1. Displacement field for the case that one crack lies along the interface of bimaterials

As illustrated in Fig. 1, a two-dimensional bimaterial domain Ω with an external boundary Γ is considered here. The solid consists of two dissimilar isotropic materials. We label the material above the interface as material 1 and below as material 2. Surface tractions $\bar{\boldsymbol{t}}$ are applied on Neumann boundaries Γ_t, whereas prescribed displacements $\bar{\boldsymbol{u}}$ are imposed on the complementary Dirichlet boundaries Γ_u, with $\Gamma_t \cap \Gamma_u = \varnothing$ and $\overline{\Gamma_t \bigcup \Gamma_u} = \Gamma$. We assume that the traction-free crack denoted as Γ_c is along the bimaterial interface. The unbroken interface is denoted as Γ_{intf}. A local polar coordinate system with origin at the crack tip is defined as (r, θ).

The coefficients E_m and ν_m denote the Young's modulus and the Poisson's ratio of the mth material $m = (1, 2)$, respectively. The corresponding shear modulus μ_m and Kolosov constant κ_m are given by

$$\mu_m = \frac{E_m}{2\left(1+\nu_m\right)} \quad \text{and} \quad \kappa_m = \begin{cases} 3-4\nu_m & \text{for plane strain} \\ \frac{3-\nu_m}{1+\nu_m} & \text{for plane stress} \end{cases}, \quad m = 1, 2\ . \tag{1}$$

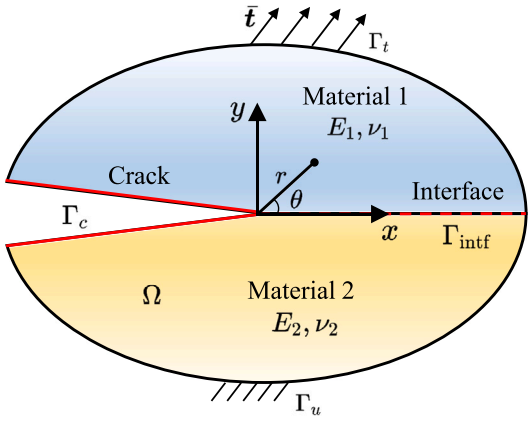

Fig. 1. An interface crack Γ_c between two dissimilar isotropic materials.

For the interface crack Γ_c, the Cartesian components $\{u, v\}$ of the corresponding asymptotic displacement field $\boldsymbol{u}$ are [17,48]:

$$\boldsymbol{u} = \begin{Bmatrix} u \\ v \end{Bmatrix} = \sum_{n=1}^{\infty} \frac{r^{n/2}}{\sqrt{2\pi}} \left[\mathrm{Re}\left(\mathrm{K}_n r^{\mathrm{i}\varepsilon_n}\right) \begin{Bmatrix} u_n^{\mathrm{I}}(\theta) \\ v_n^{\mathrm{I}}(\theta) \end{Bmatrix} + \mathrm{Im}\left(\mathrm{K}_n r^{\mathrm{i}\varepsilon_n}\right) \begin{Bmatrix} u_n^{\mathrm{II}}(\theta) \\ v_n^{\mathrm{II}}(\theta) \end{Bmatrix} \right], \tag{2}$$

where

$$\varepsilon_n = \begin{cases} \varepsilon = \frac{1}{2\pi} \log \frac{\mu_2\kappa_1+\mu_1}{\mu_1\kappa_2+\mu_2}, & n = 1,3,5,\ldots \\ 0, & n = 2,4,6,\ldots \end{cases}. \tag{3}$$

$\mathrm{Re}(\cdot)$ and $\mathrm{Im}(\cdot)$ here denote the real and imaginary parts of a complex number, respectively. K_n are complex numbers reflecting the orders of SIFs, and the ε_n is a constant or zero depending on the material properties. $r^{\mathrm{i}\varepsilon_n}$ is oscillatory with an expansion as

$$r^{\mathrm{i}\varepsilon_n} = e^{\mathrm{i}\varepsilon_n \log r} = \cos\left(\varepsilon_n \log r\right) + \mathrm{i}\sin\left(\varepsilon_n \log r\right), \tag{4}$$

where i is the imaginary unit and $\mathrm{i} = \sqrt{-1}$. In view of (3), it is clear that only the odd terms in the displacement expansions give rise to oscillatory behaviors. The nth order angular functions $\left(u_n^{\mathrm{I}}, v_n^{\mathrm{I}}\right)$ and $\left(u_n^{\mathrm{II}}, v_n^{\mathrm{II}}\right)$ are in terms of θ and given as follows [18,48]:

1. n is odd $(1,3,5,\ldots)$

$$u_n^{\mathrm{I}}(\theta) = -\frac{1}{2\mu\left(n^2+4\varepsilon^2\right)\cosh(\pi\varepsilon)} \Big\{ n\left[e^{\varepsilon(\Pi-\theta)} - \kappa e^{-\varepsilon(\Pi-\theta)}\right]\cos\frac{n}{2}\theta + \left(n^2+4\varepsilon^2\right)e^{-\varepsilon(\Pi-\theta)}\sin\theta\sin\frac{n-2}{2}\theta + 2\varepsilon\left[e^{\varepsilon(\Pi-\theta)} + \kappa e^{-\varepsilon(\Pi-\theta)}\right]\sin\frac{n}{2}\theta \Big\}, \tag{5a}$$

$$v_n^{\mathrm{I}}(\theta) = \frac{1}{2\mu\left(n^2+4\varepsilon^2\right)\cosh(\pi\varepsilon)} \Big\{ n\left[e^{\varepsilon(\Pi-\theta)} + \kappa e^{-\varepsilon(\Pi-\theta)}\right]\sin\frac{n}{2}\theta - \left(n^2+4\varepsilon^2\right)e^{-\varepsilon(\Pi-\theta)}\sin\theta\cos\frac{n-2}{2}\theta - 2\varepsilon\left[e^{\varepsilon(\Pi-\theta)} - \kappa e^{-\varepsilon(\Pi-\theta)}\right]\cos\frac{n}{2}\theta \Big\}, \tag{5b}$$

$$u_n^{\mathrm{II}}(\theta) = \frac{1}{2\mu\left(n^2+4\varepsilon^2\right)\cosh(\pi\varepsilon)} \Big\{ n\left[e^{\varepsilon(\Pi-\theta)} + \kappa e^{-\varepsilon(\Pi-\theta)}\right]\sin\frac{n}{2}\theta + \left(n^2+4\varepsilon^2\right)e^{-\varepsilon(\Pi-\theta)}\sin\theta\cos\frac{n-2}{2}\theta - 2\varepsilon\left[e^{\varepsilon(\Pi-\theta)} - \kappa e^{-\varepsilon(\Pi-\theta)}\right]\cos\frac{n}{2}\theta \Big\}, \tag{5c}$$

$$v_n^{\Pi}(\theta) = \frac{1}{2\mu\left(n^2+4\varepsilon^2\right)\cosh(\pi\varepsilon)} \Big\{ n\left[e^{\varepsilon(\Pi-\theta)} - \kappa e^{-\varepsilon(\Pi-\theta)}\right]\cos\frac{n}{2}\theta - \left(n^2+4\varepsilon^2\right)e^{-\varepsilon(\Pi-\theta)}\sin\theta\sin\frac{n-2}{2}\theta + 2\varepsilon\left[e^{\varepsilon(\Pi-\theta)} + \kappa e^{-\varepsilon(\Pi-\theta)}\right]\sin\frac{n}{2}\theta \Big\}. \tag{5d}$$

2. n is even $(2,4,6,\ldots)$

$$u_n^{\mathrm{I}}(\theta) = \frac{1}{\mu n(1+\omega)}\left[(\kappa+1)\cos\frac{n}{2}\theta - n\sin\theta\sin\frac{n-2}{2}\theta\right], \tag{6a}$$

$$v_n^{\mathrm{I}}(\theta) = \frac{1}{\mu n(1+\omega)}\left[(\kappa-1)\sin\frac{n}{2}\theta - n\sin\theta\cos\frac{n-2}{2}\theta\right], \tag{6b}$$

$$u_n^{\mathrm{II}}(\theta) = \frac{1}{\mu n(1+\omega)}\left[(\kappa-1)\sin\frac{n}{2}\theta + n\sin\theta\cos\frac{n-2}{2}\theta\right], \tag{6c}$$

$$v_n^{\mathrm{II}}(\theta) = \frac{1}{\mu n(1+\omega)}\left[-(\kappa+1)\cos\frac{n}{2}\theta - n\sin\theta\sin\frac{n-2}{2}\theta\right]. \tag{6d}$$

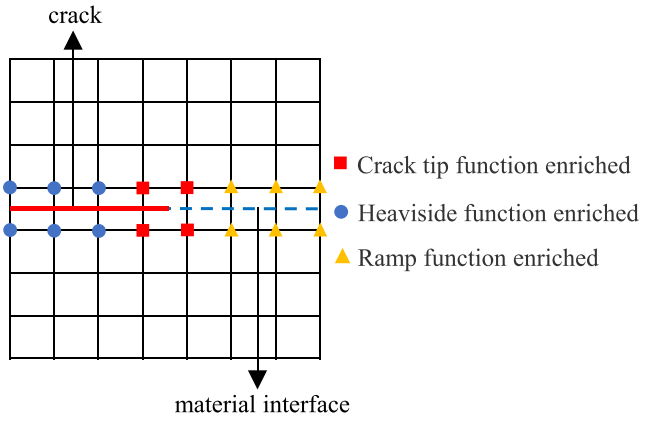

Fig. 2. A typical grid in the X-FEM with enriched nodes for a bimaterial interface crack.

The values of Π and the material constants μ, κ and ω are defined as:

$$\begin{aligned} &\Pi = \pi, \mu = \mu_1, \kappa = \kappa_1, \omega = \frac{(\kappa_1 + 1)\,\mu_2}{(\kappa_2 + 1)\,\mu_1} \quad \text{for Material 1} \\ &\Pi = -\pi, \mu = \mu_2, \kappa = \kappa_2, \omega = \frac{(\kappa_2 + 1)\,\mu_1}{(\kappa_1 + 1)\,\mu_2} \quad \text{for Material 2} \end{aligned} . \tag{7}$$

It is reminded that we here only consider the displacement with low-order singularity (i.e. $n = 1$) and have $\mathrm{K}_1 = K_\mathrm{I} + \mathrm{i}K_\mathrm{II}$. It is also important to realize that no specific length or load is specified for the displacement fields [20]. Singular fields are sought to satisfy continuity of traction and displacement vectors across the bonded portion of the interface, as well as the traction-free condition along the crack faces.

2.2. Approximation of displacement field within X-FEM

As shown in Fig. 2, the nodes in the grid of the X-FEM can be grouped into several sets according to the relative locations with the crack. $\mathcal{N}$, $\mathcal{N}_{\mathrm{cr}}$, $\mathcal{N}_{\mathrm{tip}}$ and $\mathcal{N}_{\mathrm{intf}}$ are the sets of all nodes, Heaviside function enriched nodes, crack tip function enriched nodes and ramp function enriched nodes of bimaterial, respectively.

The approximations of displacement for elastic materials in terms of different enrichments using the partition of unity are:

$$\boldsymbol{u}^h_{\mathrm{std}}(\boldsymbol{x}) = \sum_{I\in\mathcal{N}} N_I(\boldsymbol{x})\,\boldsymbol{u}_I, \tag{8}$$

$$\boldsymbol{u}^h_{\mathrm{cr}}(\boldsymbol{x}) = \sum_{I\in\mathcal{N}_{\mathrm{cr}}} N_I(\boldsymbol{x})\left[H(\boldsymbol{x}) - H\left(\boldsymbol{x}_I\right)\right]\boldsymbol{a}_I, \tag{9}$$

$$\boldsymbol{u}^h_{\mathrm{tip}}(\boldsymbol{x}) = \sum_{I\in\mathcal{N}_{\mathrm{tip}}} N_I(\boldsymbol{x}) \sum_{\alpha=1}^{12}\left[B_\alpha(\boldsymbol{x}) - B_\alpha\left(\boldsymbol{x}_I\right)\right]\boldsymbol{b}_{\alpha I}, \tag{10}$$

$$\boldsymbol{u}^h_{\mathrm{intf}}(\boldsymbol{x}) = \sum_{I\in\mathcal{N}_{\mathrm{intf}}} N_I(\boldsymbol{x})\,G(\boldsymbol{x})\boldsymbol{c}_I, \tag{11}$$

where $N_I(\boldsymbol{x})$ are finite element shape functions, while $\boldsymbol{u}_I$, $\boldsymbol{a}_I$, $\boldsymbol{b}_{\alpha I}$ and $\boldsymbol{c}_I$ are the unknowns. $H(\boldsymbol{x})$ is the generalized Heaviside function to capture the displacement jump across the crack surface, and defined as:

$$H(\boldsymbol{x}) = \begin{cases} +1 & \text{above} \quad \Gamma_c \\ -1 & \text{below} \quad \Gamma_c \end{cases} . \tag{12}$$

The asymptotic crack tip enriched functions $B_\alpha(\boldsymbol{x})$ $(\alpha = 1, 2, \ldots, 12)$ are characteristic functions derived from the analytical solution of the displacement shown in (2) [11]:

$$\begin{aligned} \left[B_\alpha(\boldsymbol{x})\right]_{\alpha=1,2,\ldots,12} = \Big[&\sqrt{r}\cos(\varepsilon\log r)\mathrm{e}^{-\varepsilon\theta}\sin\frac{\theta}{2},\ \sqrt{r}\cos(\varepsilon\log r)\mathrm{e}^{-\varepsilon\theta}\cos\frac{\theta}{2},\ \sqrt{r}\cos(\varepsilon\log r)\mathrm{e}^{\varepsilon\theta}\sin\frac{\theta}{2}, \\ &\sqrt{r}\cos(\varepsilon\log r)\mathrm{e}^{\varepsilon\theta}\cos\frac{\theta}{2},\ \sqrt{r}\cos(\varepsilon\log r)\mathrm{e}^{\varepsilon\theta}\sin\frac{\theta}{2}\sin\theta,\ \sqrt{r}\cos(\varepsilon\log r)\mathrm{e}^{\varepsilon\theta}\cos\frac{\theta}{2}\sin\theta, \\ &\sqrt{r}\sin(\varepsilon\log r)\mathrm{e}^{-\varepsilon\theta}\sin\frac{\theta}{2},\ \sqrt{r}\sin(\varepsilon\log r)\mathrm{e}^{-\varepsilon\theta}\cos\frac{\theta}{2},\ \sqrt{r}\sin(\varepsilon\log r)\mathrm{e}^{\varepsilon\theta}\sin\frac{\theta}{2}, \\ &\sqrt{r}\sin(\varepsilon\log r)\mathrm{e}^{\varepsilon\theta}\cos\frac{\theta}{2},\ \sqrt{r}\sin(\varepsilon\log r)\mathrm{e}^{\varepsilon\theta}\sin\frac{\theta}{2}\sin\theta,\ \sqrt{r}\sin(\varepsilon\log r)\mathrm{e}^{\varepsilon\theta}\cos\frac{\theta}{2}\sin\theta\Big] . \end{aligned} \tag{13}$$

Note that the bimaterial constant is $\varepsilon = 0$ for homogeneous materials. In this situation, the 12 branching functions degrade to 4 independent functions as follows:

$$\left[B_\alpha(\boldsymbol{x})\right]_{\alpha=1,2,3,4} = \left[\sqrt{r}\sin\frac{\theta}{2}, \sqrt{r}\cos\frac{\theta}{2}, \sqrt{r}\sin\frac{\theta}{2}\sin\theta, \sqrt{r}\cos\frac{\theta}{2}\sin\theta\right]. \tag{14}$$

These functions are widely used to capture the asymptotic features at the crack tip of homogeneous materials [6,7].

The approximation of displacement insofar is complete [11,15,17,18], as:

$$\boldsymbol{u}^h(\boldsymbol{x}) = \boldsymbol{u}^h_{\text{std}}(\boldsymbol{x}) + \boldsymbol{u}^h_{\text{cr}}(\boldsymbol{x}) + \boldsymbol{u}^h_{\text{tip}}(\boldsymbol{x}). \tag{15}$$

Remind that the weak discontinuity along the material interface can be modeled by a ramp enrichment function $G(\boldsymbol{x})$ defined as [49]:

$$G(\boldsymbol{x}) = \sum_{I\in\mathcal{N}_{\text{intf}}} |\Psi_I| N_I(x) - \left|\sum_{I\in\mathcal{N}_{\text{intf}}} \Psi_I N_I(x)\right|, \tag{16}$$

where Ψ_I is the shortest signed distance of the node I to the material interface and $\|\cdot\|$ is the Euclidean norm. The shortest signed distance is defined as:

$$\Psi(\boldsymbol{x}) = \text{sign}\,(\boldsymbol{n}\cdot(\boldsymbol{x}-\bar{\boldsymbol{x}})) \min_{\bar{\boldsymbol{x}}\in\Gamma_{\text{intf}}} \|\boldsymbol{x}-\bar{\boldsymbol{x}}\|, \tag{17}$$

where $\boldsymbol{n}$ is the outward normal to the interface Γ_{intf} and $\text{sign}(\cdot)$ is the sign operator. Therefore, there is another enriching scheme as [12,19]:

$$\boldsymbol{u}^h(\boldsymbol{x}) = \boldsymbol{u}^h_{\text{std}}(\boldsymbol{x}) + \boldsymbol{u}^h_{\text{cr}}(\boldsymbol{x}) + \boldsymbol{u}^h_{\text{tip}}(\boldsymbol{x}) + \boldsymbol{u}^h_{\text{intf}}(\boldsymbol{x}). \tag{18}$$

We here first examine the effect of the $\boldsymbol{u}^h_{\text{intf}}(\boldsymbol{x})$.

2.3. Computation θ for curved fractures

We should keep in mind that $\theta = \pi$ and $\theta = -\pi$ require to represent the positive and negative surface of the crack even with curvature. As shown in Fig. 3, the blue solid curve represents a crack. For a given point A, if we directly determine its r and θ in terms of the local Cartesian coordinate system, it may introduces inconsistency. Specifically, if the A lies on the curved crack, θ cannot maintain $\pm\pi$. Such inconsistency may severely impair the accuracy and convergence of the X-FEM. In order to use the enrichment for cracks with arbitrary geometries, the polar coordinate θ should be determined in a curvilinear coordinate system that satisfies two conditions: (i) θ takes the values π on the upper crack surface or $-\pi$ on the lower crack surface; (ii) it can automatically degenerate to a Cartesian reference system in case of straight cracks [50]. To fulfill both conditions, the signed-distance function to the crack ψ, can be read

$$\psi(\boldsymbol{x}) = \text{sign}\,(\boldsymbol{n}\cdot(\boldsymbol{x}-\bar{\boldsymbol{x}})) \min_{\bar{\boldsymbol{x}}\in\Gamma_c\cup\Gamma_{ce}} \|\boldsymbol{x}-\bar{\boldsymbol{x}}\|, \tag{19}$$

where $\boldsymbol{n}$ is the outward normal to the crack surface, Γ_c is the crack surface and Γ_{ce} is the tangential extension of the crack surface. This signed distance can determine the location of crack surface, but we need one more function $\varphi(\boldsymbol{x})$ to locate the crack front, which is defined as:

$$\varphi(\boldsymbol{x}) = \text{sign}\left(\boldsymbol{t}\cdot\left(\boldsymbol{x}-\boldsymbol{x}_t\right)\right)\sqrt{r^2-\psi^2}, \tag{20}$$

where $\boldsymbol{t}$ is the unit vector tangent to the crack surface at the crack tip holding the position of $\boldsymbol{x}_t$, r is the distance between the given point and the crack tip. The angle $\theta(\boldsymbol{x})$ thus can be calculated as:

$$\theta(\boldsymbol{x}) = \arctan\left(\frac{\psi(\boldsymbol{x})}{\varphi(\boldsymbol{x})}\right). \tag{21}$$

Once θ is determined, the curvilinear coordinate system for the point can be given as follows. As shown in Fig. 3, we first calculate ψ and φ at point A according to (19) and (20), where $AA' = AA''$ and $AA'' \perp TA''$. We then rotate AT with $-\theta$ at point T to obtain the x_1 axis. The corresponding coordinate system for the point A thus can be computed.

As an example, we consider a quarter of a circle. Fig. 4 shows the distributions of $\psi(\boldsymbol{x})$, $\varphi(\boldsymbol{x})$, and $\theta(\boldsymbol{x})$. We can see that θ jumps from $-\pi$ to $+\pi$ across the true crack surface. We further applied the above algorithm to two types of curves with different levels of continuity: a curve composed of line segments and a curve in sine form. The computed θ comes out as expected. In this sense, the algorithm is applicable to continuous curved cracks, and smoothness is not a requirement..

3. SIFs computation

As reviewed in the introduction, there are mainly three extraction methods of SIFs, e.g. IIM, CIM and DCM. In this section, we describe these methods.

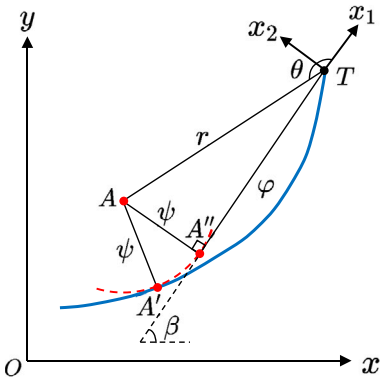

Fig. 3. Signed distances for a given point A and its coordinate system at the crack tip.

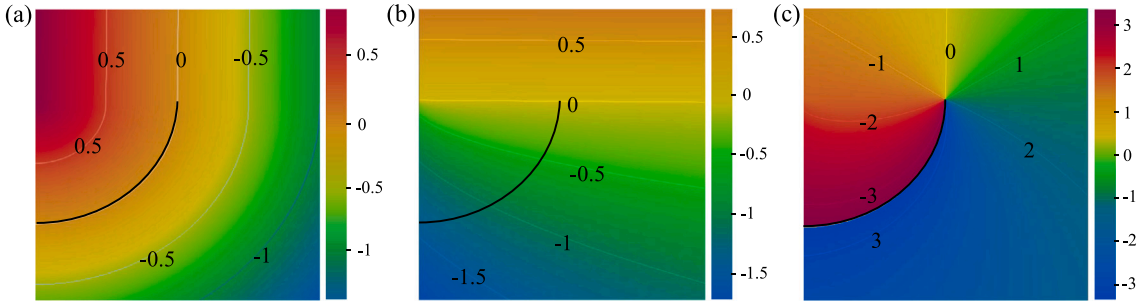

Fig. 4. Contours for a circular arc crack represented by black lines: (a) $\psi(\boldsymbol{x})$, (b) $\varphi(\boldsymbol{x})$, and (c) $\theta(\boldsymbol{x})$.

3.1. The interaction integral method

To start, a general two-dimensional contour integration, called as J-integral, is defined as [38]:

$$J = \int_{\Gamma_A} P_{1j} n_j \, \mathrm{d}\Gamma_A, \tag{22}$$

where $P_{1j} = \frac{1}{2}\sigma_{ik}\varepsilon_{ik}\delta_{1j} - \sigma_{ij}u_{i,1}$, with σ_{ij} and ε_{ij} representing the components of stress and strain tensors, respectively, the subscript 1 representing the x-direction in two-dimensional, δ_{1j} representing the Kronecker symbol, and $u_{i,1}$ representing the gradient along x-axis of the displacement. We here adopt the convention of Einstein summation. Γ_A is an arbitrarily closed path around the crack tip and n_j denotes the outward normal vector along Γ_A. It is well-known that the J-integral is path-independent for cracks in homogeneous materials, and for heterogeneous material, this conclusion is still valid when the crack lies along the interface [51], which is the studied case. The J-integral therefore can be employed to extract SIFs in this work.

In the IIM, auxiliary fields are required to be introduced and superposed on the actual fields that arise from the solution of the boundary-value problem. By judicious choice of the auxiliary fields, the interaction integral can be directly related to the SIFs. One of the choices for the auxiliary state is the displacement and stress fields in the vicinity of the interface crack-tip as shown in (2). The J-integral for the sum of the two states can be defined as:

$$J = J^{\mathrm{act}} + J^{\mathrm{aux}} + I, \tag{23}$$

where J^{act} and J^{aux} are associated with the actual and auxiliary states, respectively, and I is the interaction integral defined as [52]:

$$I = \int_{\Gamma_A} \left(\sigma_{ik}\varepsilon_{ik}^{\mathrm{aux}}\delta_{1j} - \sigma_{ij}u_{i,1}^{\mathrm{aux}} - \sigma_{ij}^{\mathrm{aux}}u_{i,1}\right) n_j \, \mathrm{d}\Gamma_A, \tag{24}$$

where u_i^{aux}, $\varepsilon_{ij}^{\mathrm{aux}}$ and $\sigma_{ij}^{\mathrm{aux}}$ are the auxiliary displacement, strain and stress fields, respectively. The interaction integral is related to the SIFs K_I and K_{II} through the relation [52]:

$$I = \frac{2}{E^* \cosh^2(\pi\epsilon)} \left[K_I K_I^{\mathrm{aux}} + K_{II} K_{II}^{\mathrm{aux}}\right], \tag{25}$$

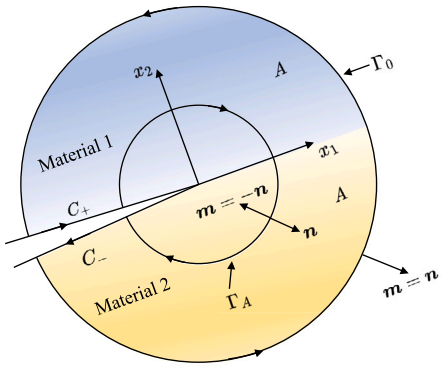

Fig. 5. Domain integral representation. Domain A is enclosed by Γ_A, C_+, C_- and Γ_0.

where K_I^{aux} and K_{II}^{aux} are local auxiliary SIFs for the auxiliary fields, respectively, and E^* is the effective Young's modulus given by

$$E^* = \frac{2E_1' E_2'}{E_1' + E_2'} \quad \text{where} \quad E' = \begin{cases} \frac{E}{1-\upsilon^2} & \text{plane strain} \\ E & \text{plane stress} \end{cases}. \tag{26}$$

The SIFs K_I and K_{II} can be computed using a proper choice of K_I^{aux} and K_{II}^{aux}. For example, by selecting $K_I^{\text{aux}} = 1$ and $K_{II}^{\text{aux}} = 0$, we can obtain the auxiliary displacement fields as shown in (2) and the corresponding distribution of stresses. We further can compute I at this state (denoted by I_1) according to (24) and K_I therefore can be computed according to (25), as:

$$K_I = \frac{E^* \cosh^2(\pi\varepsilon)}{2} I_1. \tag{27}$$

In an analogous manner, we compute I at the state with $K_I^{\text{aux}} = 0$ and $K_{II}^{\text{aux}} = 1$, denoted by I_2. We thus have:

$$K_{II} = \frac{E^* \cosh^2(\pi\varepsilon)}{2} I_2. \tag{28}$$

In a numerical implementation, as shown in Fig. 5, (24) is converted into a volume integration by multiplying the integrand by a sufficiently smooth weighting function $q(\boldsymbol{x})$ which takes a value of unity on an open set containing the crack tip and vanishes on an outer prescribed contour Γ_0. In this manner, the interaction integral along boundaries is first extended into:

$$I = \int_C \left(\sigma_{ik} \varepsilon_{ik}^{\text{aux}} \delta_{1j} - \sigma_{ij} u_{i,1}^{\text{aux}} - \sigma_{ij}^{\text{aux}} u_{i,1} \right) q m_j \, \mathrm{d}C, \tag{29}$$

where the contour $C = \Gamma_A + C_+ + C_- + \Gamma_0$ and m_j is the unit outward normal to the contour C. By using the divergence theorem and considering the equilibrium equation of the auxiliary fields, it gives the following equation for the interaction integral in a domain form [39]:

$$I = -\int_A \left(\sigma_{ik} \varepsilon_{ik}^{\text{aux}} \delta_{1j} - \sigma_{ij} u_{i,1}^{\text{aux}} - \sigma_{ij}^{\text{aux}} u_{i,1} \right) q_{,j} \, \mathrm{d}A, \tag{30}$$

where we have used the relations $m_j = -n_j$ on Γ_A and $m_j = n_j$ on C_+, C_- and Γ_0. Note that the domain region A can be only related to the outer contour Γ_0 by taking the limit as the contour Γ_A is shrunk to the crack tip.

3.2. The contour integral method

In line with the formulations derived by Hong and Stern [46] and Yang and Kuang [47], as illustrated in Fig. 6, the bimaterial SIFs of cracks lying at the interface of two dissimilar isotropic materials are given by:

$$K_I = \int_{\Gamma_2} \left(t_i \tilde{u}_i^{\text{I}} - \tilde{t}_i^{\text{I}} u_i \right) \mathrm{d}\Gamma + \int_{\Gamma_3} \hat{t}_i \tilde{u}_i^{\text{I}} \mathrm{d}\Gamma + \int_{\Gamma_4} \hat{t}_i \tilde{u}_i^{\text{I}} \mathrm{d}\Gamma, \tag{31}$$

$$K_{II} = \int_{\Gamma_2} \left(t_i \tilde{u}_i^{\text{II}} - \tilde{t}_i^{\text{I}} u_i \right) \mathrm{d}\Gamma + \int_{\Gamma_3} \hat{t}_i \tilde{u}_i^{\text{II}} \mathrm{d}\Gamma + \int_{\Gamma_4} \hat{t}_i \tilde{u}_i^{\text{II}} \mathrm{d}\Gamma, \tag{32}$$

where Γ_2 is a circular contour of radius ρ_2 centered on the crack tip that begins at one crack surface and end on the other and is away from the crack tip, Γ_3 and Γ_4 are the contours on the upper and lower crack surfaces, respectively. $\tilde{u}_i^{\text{I}}$ and $\tilde{t}_i^{\text{I}}$ are complementary displacement and traction vectors associated with K_I, $\tilde{u}_i^{\text{II}}$ and $\tilde{t}_i^{\text{II}}$ that associated with K_{II}. $\hat{t}_i$ is the applied traction vector on crack surfaces and is zero in the case of stress-free crack surfaces. t_i and u_i are traction and displacement vectors computed by any numerical technique, such as the X-FEM in this paper. For bimaterial, the complementary terms, so-called extraction functions, are listed in Appendix. Note that the integrals along curves are computed via the Gaussian quadrature scheme [43].

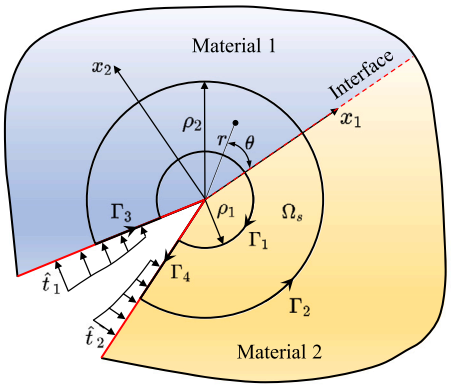

Fig. 6. Extraction path and local coordinate system for CIM.

3.3. The displacement correlation method

The DCM directly relates SIFs to the jump of displacements across the crack surface. For a bimaterial interface crack, the displacement field in the vicinity of the crack tip, i.e. (2), is reformulated as:

$$(v+\mathrm{i}u)_{\theta=\pi}=\frac{(K_I+\mathrm{i}K_{II})(1+\kappa_1)r^{\frac{1}{2}+\mathrm{i}\varepsilon}}{2\sqrt{2\pi}\mu_1(1+2\mathrm{i}\varepsilon)\cosh(\pi\varepsilon)}+c_1r^{\frac{3}{2}+\mathrm{i}\varepsilon}+O(r^{\frac{5}{2}+\mathrm{i}\varepsilon}), \tag{33}$$

$$(v+\mathrm{i}u)_{\theta=-\pi}=\frac{(K_I+\mathrm{i}K_{II})(1+\kappa_2)r^{\frac{1}{2}+\mathrm{i}\varepsilon}}{2\sqrt{2\pi}\mu_2(1+2\mathrm{i}\varepsilon)\cosh(\pi\varepsilon)}+c_2r^{\frac{3}{2}+\mathrm{i}\varepsilon}+O(r^{\frac{5}{2}+\mathrm{i}\varepsilon}). \tag{34}$$

The parameters c_1 and c_2 depend on the material properties, boundary conditions and the geometry of the domain. By introducing a new parameter c, the displacement jump thus is:

$$\Delta v+\mathrm{i}\Delta u=(v+\mathrm{i}u)_{\theta=\pi}-(v+\mathrm{i}u)_{\theta=-\pi}=\frac{(K_I+\mathrm{i}K_{II})r^{\frac{1}{2}+\mathrm{i}\varepsilon}}{2\sqrt{2\pi}(1+2\mathrm{i}\varepsilon)\cosh(\pi\varepsilon)}\left(\frac{1+\kappa_1}{\mu_1}+\frac{1+\kappa_2}{\mu_2}\right)+cr^{\frac{3}{2}+\mathrm{i}\varepsilon}+O(r^{\frac{5}{2}+\mathrm{i}\varepsilon}). \tag{35}$$

We further define:

$$\mathrm{K}^*(r):=\frac{2\sqrt{2\pi}(1+2\mathrm{i}\varepsilon)\cosh(\pi\varepsilon)}{r^{\frac{1}{2}+\mathrm{i}\varepsilon}}\frac{\mu_1\mu_2}{\left(1+\kappa_1\right)\mu_2+\left(1+\kappa_2\right)\mu_1}(\Delta v+\mathrm{i}\Delta u)=K+\tilde{c}r+\mathcal{O}\left(r^2\right), \tag{36}$$

where $\mathrm{K}=K_I+\mathrm{i}K_{II}$. Using two points along the crack surface with $r_b>r_a$, we have

$$\mathrm{K}_{r_a}=\mathrm{K}^*\left(r_a\right)=\mathrm{K}+\tilde{c}r_a,\quad \mathrm{K}_{r_b}=\mathrm{K}^*\left(r_b\right)=\mathrm{K}+\tilde{c}r_b. \tag{37}$$

Thus, K is approximated with an error of $\mathcal{O}\left(r^2\right)$ as

$$\mathrm{K}=\frac{r_b}{r_b-r_a}\left(\mathrm{K}_{r_a}-\frac{r_a}{r_b}\mathrm{K}_{r_b}\right). \tag{38}$$

In practice, we separate the real and imaginary parts in (35) and (36) to obtain

$$\begin{Bmatrix}\Delta u\\ \Delta v\end{Bmatrix}=C\begin{bmatrix}-2\varepsilon\cos(Q)+\sin(Q) & \cos(Q)+2\varepsilon\sin(Q)\\ \cos(Q)+2\varepsilon\sin(Q) & 2\varepsilon\cos(Q)-\sin(Q)\end{bmatrix}\begin{Bmatrix}K_I\\ K_{II}\end{Bmatrix}+\begin{Bmatrix}cr^{\frac{3}{2}}\sin(Q)+\sin(Q)O(r^{\frac{5}{2}})\\ cr^{\frac{3}{2}}\cos(Q)+\cos(Q)O(r^{\frac{5}{2}})\end{Bmatrix}, \tag{39}$$

where

$$C=\frac{\mu_1\left(1+\kappa_2\right)+\mu_2\left(1+\kappa_1\right)}{2\mu_1\mu_2\left(1+4\varepsilon^2\right)\cosh(\pi\varepsilon)}\sqrt{\frac{r}{2\pi}},\quad Q=\varepsilon\ln(r), \tag{40}$$

and

$$\begin{Bmatrix}K_I^*(r)\\ K_{II}^*(r)\end{Bmatrix}:=D\begin{bmatrix}-2\varepsilon\cos(Q)+\sin(Q) & \cos(Q)+2\varepsilon\sin(Q)\\ \cos(Q)+2\varepsilon\sin(Q) & 2\varepsilon\cos(Q)-\sin(Q)\end{bmatrix}\begin{Bmatrix}\Delta u\\ \Delta v\end{Bmatrix}=\begin{Bmatrix}K_I\\ K_{II}\end{Bmatrix}+\begin{Bmatrix}\tilde{c}r\sin(Q)+O(r^2)\\ \tilde{c}r\cos(Q)+O(r^2)\end{Bmatrix}, \tag{41}$$

where

$$D=\frac{2\mu_1\mu_2\cosh(\pi\varepsilon)}{\mu_1\left(1+\kappa_2\right)+\mu_2\left(1+\kappa_1\right)}\sqrt{\frac{2\pi}{r}}. \tag{42}$$

We then can approximate K using two points as shown in (37) and (38). Note that some improvements increasing accuracy include averaging scheme and linear least square extrapolation scheme. Details can be found in Gupta et al. [31].

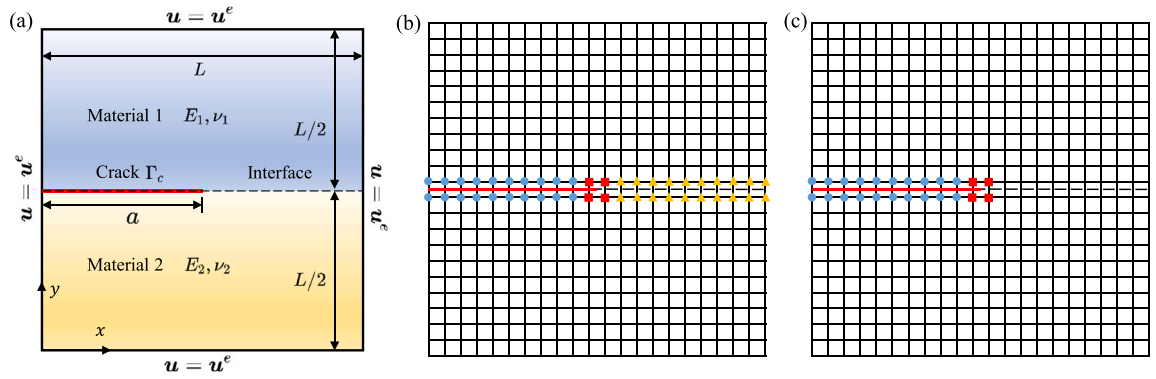

Fig. 7. Edge interface crack: (a) geometry and boundary conditions, (b) grid with 21 × 21 cells with enrichment of ramp functions (sch1), and (c) grid with 21 × 21 cells without enrichment of ramp functions (sch2). Red solid line: crack; Black dash line: interface; Red squares: nodes enriched with singular functions; Blue circles: nodes enriched with the Heaviside function; and Orange triangles: nodes enriched with the ramp function.

4. Numerical experiments

In this section, we consider three different models. The first one is the edge-crack, which has analytical solutions of the displacement field. We then conduct simulations of the slated-crack. The last example to study the non-planar crack, i.e. a circular-arc crack. For all models, we compare the enrichment schemes and the methods to extract SIFs.

4.1. An edge crack in a bimaterial sample

As shown in Fig. 7(a), we first consider an edge crack with length $a = 1$ in a square sample Ω with a length of $L = 2$. The sample consists of two dissimilar materials, and the upper is labeled as 1 and the lower 2. Elastic material parameters are: $E_1 = 1$, $E_2 = 2$, and $\nu_1 = \nu_2 = 0.3$. The crack lies on the interface. Dirichlet boundary conditions are imposed on the whole boundary as: $\boldsymbol{u}(\boldsymbol{x}) = \bar{\boldsymbol{u}}(\boldsymbol{x})$ $\forall \boldsymbol{x} \in \partial\Omega$, where $\bar{\boldsymbol{u}}(\boldsymbol{x})$ is calculated by (2) setting $K_I = K_{II} = 1$. We thus can obtain the analytical displacement field for the whole domain $\boldsymbol{u}^e(\boldsymbol{x})$ $\forall \boldsymbol{x} \in \Omega$ given as (2) and the exact solution of SIFs $K_I^e = K_{II}^e = 1$. Note that the plane-strain assumption is adopted here. We here use rectangular cells to discretize the domain, and the cell size is denoted as h.

4.1.1. Enrichment schemes

We first check the effects of different enrichment schemes. As shown in Fig. 7(b–c), enrichment schemes with and without the ramp function along the interface are compared, while constantly keep one layer of elements around the crack tip enriched with singular functions. The enrichment with ramp function is denoted to "sch1", and without ramp function to "sch2". Four different mesh sizes, i.e. $21 \times 21, 51 \times 51, 101 \times 101$ and 151×151 elements, are employed to conduct convergence analyses. Relative error in energy norm, condition number of the stiffness matrix, and relative error in SIFs are compared for different schemes.

1. Error of energy. The relative error in the energy norm is defined as [11,18]:

$$E_\Omega = \sqrt{\frac{\int_\Omega \left(\boldsymbol{\varepsilon}^e - \boldsymbol{\varepsilon}^h\right)^{\mathrm{T}} \mathbf{C} \left(\boldsymbol{\varepsilon}^e - \boldsymbol{\varepsilon}^h\right) \mathrm{d}\Omega}{\int_\Omega \left(\boldsymbol{\varepsilon}^e\right)^{\mathrm{T}} \mathbf{C} \left(\boldsymbol{\varepsilon}^e\right) \mathrm{d}\Omega}}, \tag{43}$$

   where $\boldsymbol{\varepsilon}$ denotes the strain fields and the superscripts e and h refer to the exact and numerical solutions, respectively; $\mathbf{C}$ is the elasticity matrix that relates the strains with the stresses.
2. Condition number. To assess the conditioning of the X-FEM system matrix $\mathbf{K}$, the scaled condition number $\mathcal{R}$ is adopted [18, 53]:

$$\mathcal{R}(\mathbf{K}) = \hat{\kappa}_2\left(\mathbf{D}^{\mathrm{T}}\mathbf{K}\mathbf{D}\right), \tag{44}$$

   where $\mathbf{D}$ is a diagonal matrix defined as $\mathbf{D} = \sqrt{\mathrm{diag}(\mathbf{K})^{-1}}$ and $\hat{\kappa}_2(\cdot)$ denotes the condition number based on $\|\cdot\|_2$ vector norm. In this manner, the scaled condition number is smaller than the original one.
3. Error of SIFs. We here employ the IIM to calculate SIFs for different enriching schemes. Discussions of computation of SIFs will be given in the next subsection.

As results, Table 1 summarizes the indicators comparing the different enriching schemes. We can see that sch1 is more accurate than sch2 in terms of the energy norm, but the two enrichment schemes are almost identical for condition numbers and SIFs. This reflects that the enrichment with ramp functions can improve the accuracy at regions far from the tip, which is expected.

Additionally, we visualize the convergence rates in Fig. 8, which shows the relative error in the energy norm E_Ω and scaled condition numbers $\mathcal{R}(\mathbf{K})$ as functions of the element size. The same conclusions can be drawn via these figures.

Table 1
Indicators for the edge interface crack problem.

Scheme	Mesh	Relative error E_Ω	Condition number $\mathcal{R}$	K_I	K_{II}
sch1	21 × 21	0.118859	1.2134×10^8	0.999611	0.988451
	51 × 51	0.0740368	2.1428×10^8	0.999673	0.99573
	101 × 101	0.0515229	3.0446×10^8	0.999647	0.998044
	151 × 151	0.0416404	3.6675×10^8	0.999632	0.998787
sch2	21 × 21	0.141145	1.2120×10^8	1.00032	0.988296
	51 × 51	0.0922902	2.1403×10^8	0.999074	0.992934
	101 × 101	0.0664553	3.0412×10^8	0.998567	0.994113
	151 × 151	0.0547566	3.6634×10^8	0.998397	0.994432

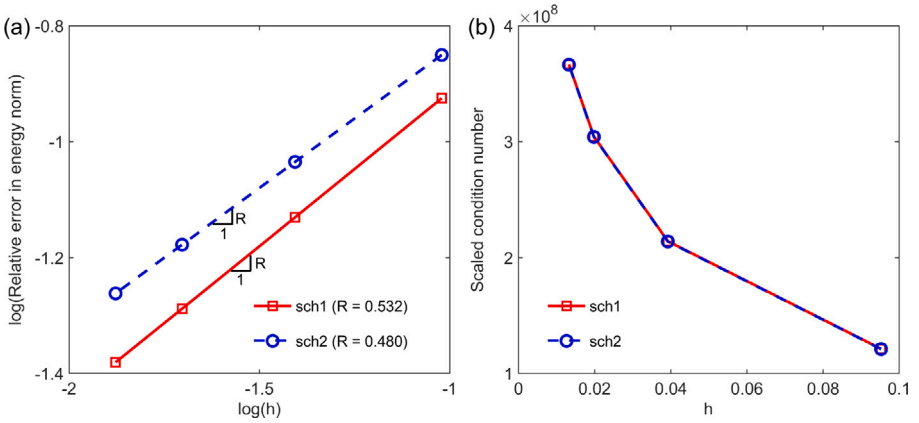

Fig. 8. Comparisons of (a) error of energy norm and (b) scaled condition number for different enrichment schemes.

4.1.2. Extraction of the SIFs

Since sch1 is more accurate than sch2 for the edge problem, we employ the sch1 for the enriching scheme and now compare the computational methods for the SIFs. As adopted in Gupta et al. [31], the extraction parameter ρ is individually defined as:

1. IIM: $\rho = r_d/h$, where r_d is contour domain radius and h is the crack tip element size;
2. CIM: $\rho = \rho_2/h$, where ρ_2 is the outer radius of the extraction domain as shown in Fig. 6;
3. DCM: $\rho = r_a/h$, where r_a and r_b ($r_a < r_b$) are the locations of the extracting points as shown in (38).

We compare the numerical results and the exact values in a relative manner, as:

$$e^r = \left| \frac{\text{Numerical} - \text{Exact}}{\text{Exact}} \right|. \tag{45}$$

Fig. 9 compares the relative error of SIFs with ρ for different methods, i.e. IIM, CIM and DCM, where $\Delta = r_b - r_a = 0.1h$ holds for the DCM. We can see that the IIM is the most accurate and robust method to extract SIFs (both for the K_I and K_{II}). Conversely, we should carefully choose the extraction parameters for the DCM. To some extent, the CIM is not so sensitive to ρ and provides not so accurate but acceptable results.

We next discuss the choice of the parameters for the DCM considering the distance between the extracting points Δ and interpolation strategies. Fig. 10 shows the sensitivities of Δ to the SIFs. We can see that both the maximum errors and oscillations of the SIFs decrease with Δ increasing. Fixed the beginning and ending extraction points, we then use 11 points to extract the SIFs. The averaging scheme and linear scheme [31] (using an extrapolation based on the moving least square method to obtain the value at $r = 0$) are compared with the two points method. As shown in Fig. 11, the averaging scheme using multiple points can improve the accuracy of the DCM.

In a summary, we set $\rho = 3$ and $\rho = 4.5$ for the IIM and the CIM, respectively. $\Delta = 0.1h$, $\rho = 10$, and an averaging scheme using 11 extracting points are adopted to the DCM.

Using these optimized extraction parameter, we compute the SIFs with different ratios of moduli, e.g. $E_2/E_1 = 2, 10$ and 100. As shown in Table 2, the calculated results are in agreement with the exact solutions.

4.2. A center crack in a slanted bimaterial sample

We now adopt the parameters optimized in the last example to check their effectiveness to a plane crack problem. As shown in Fig. 12(a), a center slanted crack embedded a finite bimaterial sample is employed, and the sample is subjected to a uniaxial uniform tension σ. The crack also lies on the interface (represented by the red dot line) of two dissimilar materials. The width and

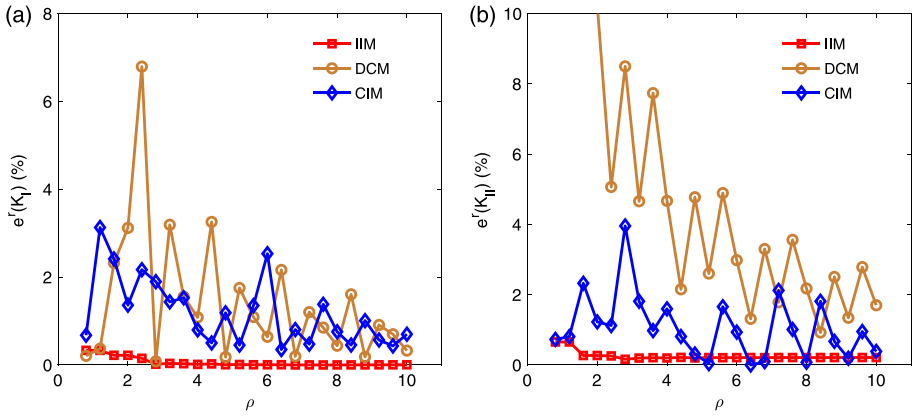

Fig. 9. The relative errors of SIFs (a) K_I and (b) K_{II} with the characteristic length of the extraction zone ρ for different methods.

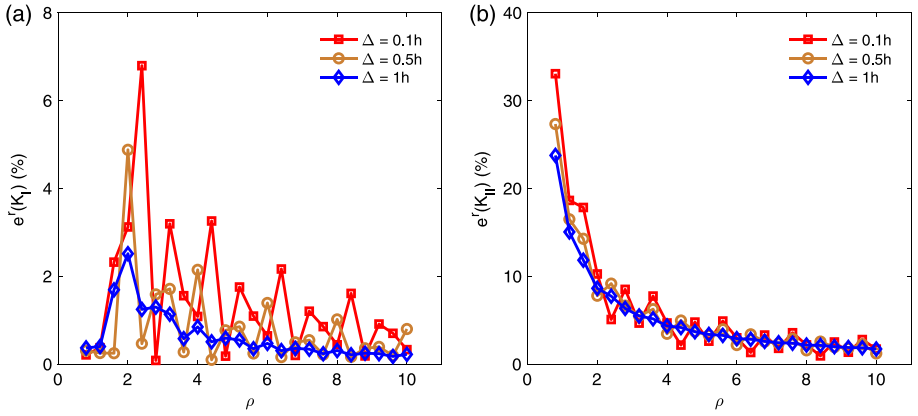

Fig. 10. Sensitivities of the distance between sampling points to the SIFs.

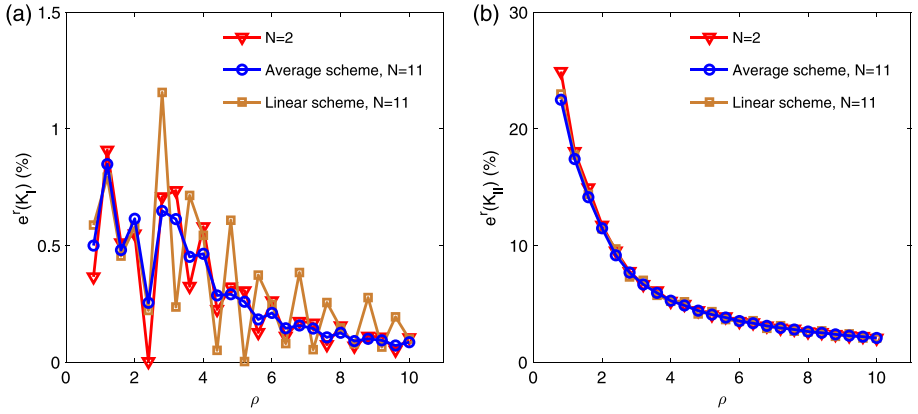

Fig. 11. Strategies of extraction methods of the DCM.

height of the sample is $2L$ and $4L$, respectively, and the length of the crack is $a = 0.5L$. We here set $L = 1$ and $\sigma = 1$. The material constants are $E_1/E_2 = 10$, and $\nu_1 = \nu_2 = 0.3$. The slope angle α can vary from 0° to 90°.

4.2.1. Validation of the X-FEM code for planar cracks

We first validate our X-FEM code, which is developed on the platform of dealii [54]. The same configuration with $\alpha = 15°$ is adopted to simulate using the ABAQUS software based on the FEM. We compare our results with the results of the ABAQUS in terms of the displacement along y-direction. As shown in Fig. 13, we can see the distributions of the displacement are identical.

Table 2
SIFs for the edge crack problem with different ratios of moduli.

E_1/E_2	K_I				K_{II}			
	Exact	IIM	CIM	DCM	Exact	IIM	CIM	DCM
2	1	0.999647	1.00645	0.999143	1	0.998044	0.995419	1.00208
10	1	0.998196	0.998536	1.00069	1	0.999836	0.998175	1.00539
100	1	0.997626	0.99727	1.00555	1	1.00162	0.997433	0.993239

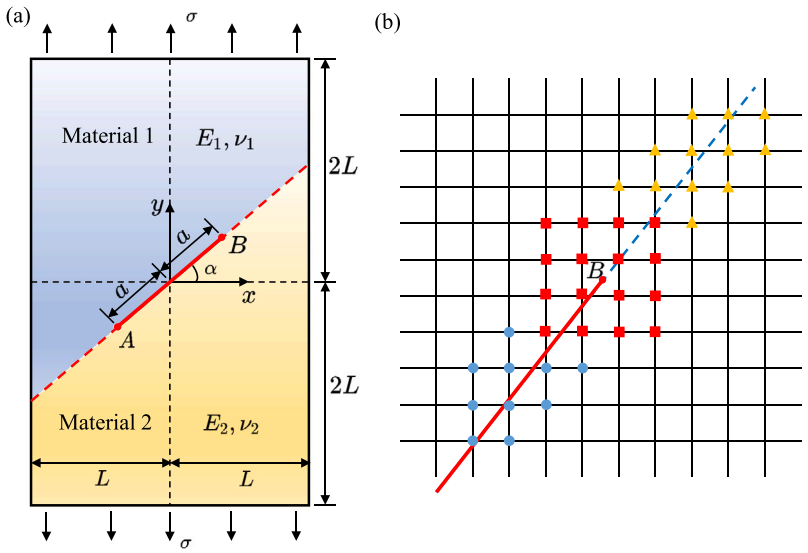

Fig. 12. A center crack embedded in a slanted bimaterial sample: (a) geometry and boundary conditions; (b) enriched nodes.

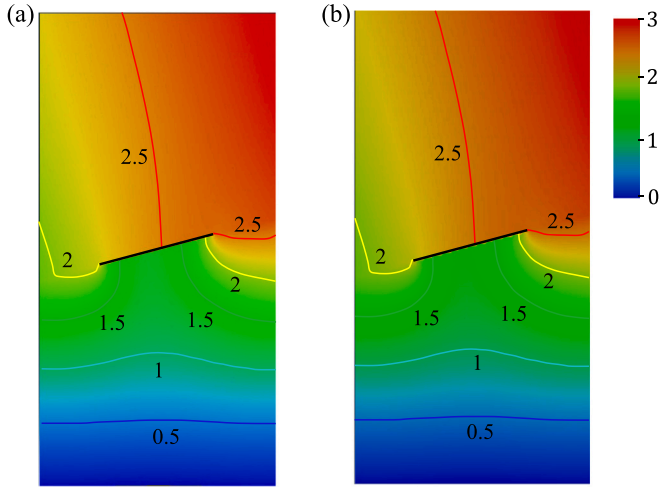

Fig. 13. Comparison of displacement fields along y direction for a slanted crack problem (a) ABAQUS and (b) X-FEM.

4.2.2. Enrichment schemes

We here further check the effects of different enriching schemes, i.e. with and without ramp functions. The slope angle is fixed at $\alpha = 15°$. Four different mesh sizes, e.g. $11 \times 21, 21 \times 41, 41 \times 81$, 51×101 and 81×161 elements, are employed to conduct convergence analyses. The relative error of displacement is measured as:

$$E_{L_2} = \frac{\|\boldsymbol{u}^r - \boldsymbol{u}^h\|}{\|\boldsymbol{u}^r\|}, \tag{46}$$

where $\|\boldsymbol{u}^r\|$ is the L_2 norm of reference solution and $\|\boldsymbol{u}^h\|$ is that of the approximated solution. Since there is no analytical solution for this problem, we here use results with finest meshes as the exact solution of displacements. This treatment is reasonable since

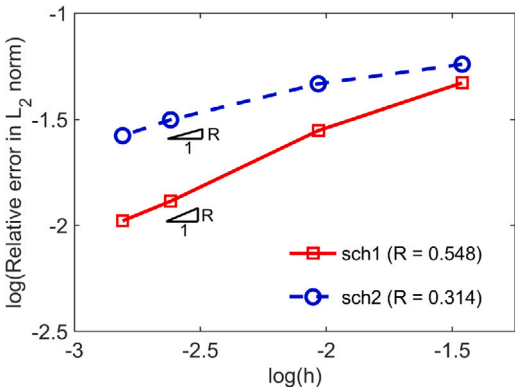

Fig. 14. Relative error in L_2 norm using different enrichment schemes.

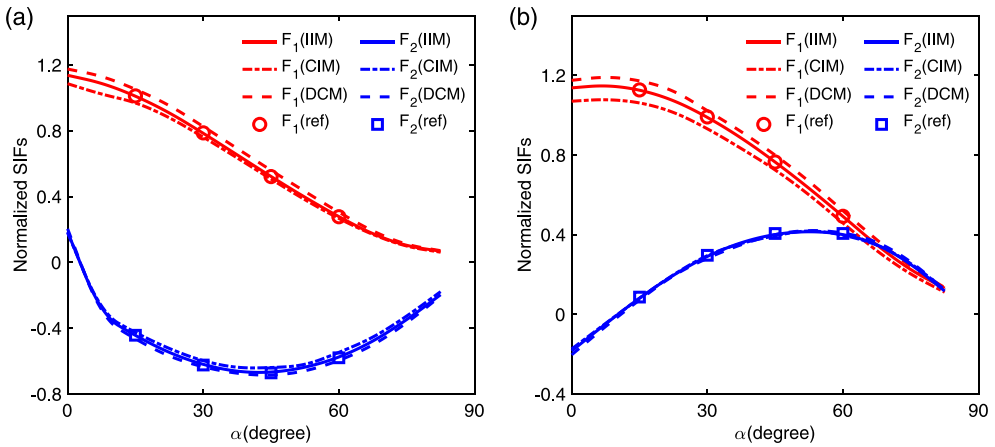

Fig. 15. Normalized SIFs at the (a) left and (b) right crack tip of the center crack problem with $E_1/E_2 = 10$.

the relative error in L_2 norm of the two enrichment schemes with the finest meshes (81 × 161 elements) is less than 0.5%. Fig. 14 compares the convergence rate of different enrichment schemes. As expected, the enrichment with ramp functions holds faster convergence rate and lower relative error than enrichment without ramp functions.

4.2.3. Extraction of the SIFs

As discussed above, we adopt the first enrichment scheme to conduct simulations. As shown in Fig. 12(b), we here enrich the nodes among the nearest two layer of elements at the crack tip with singular functions to obtain accurate SIFs. The computed SIFs is normalized for comparisons, as:

$$F_1 = \frac{K_{\mathrm{I}}}{\sigma\sqrt{\pi a}}, \quad F_2 = \frac{K_{\mathrm{II}}}{\sigma\sqrt{\pi a}}. \tag{47}$$

Fig. 15 plots the curves of the nondimensional SIFs with the inclination angle α for different extraction methods. The reference solution is reported in [35]. We can see that using the optimized extraction parameters, all three extraction methods can reflect the relationship of SIFs with the slope angle. It is noted that we employ the singular functions with an accuracy of $\sqrt{r}$ and only one-order shape functions. It may introduce an error to the displacement field, especially for coarse cells. The displacement jump across the crack surface may be affected by the approximation, which influences the accuracy of DCM. The energy-based methods (i.e., the CIM and the IIM) are not so sensitive to the accuracy of displacement. In practice, we approximate the contours of CIM as line segments, and such discretization may introduce errors. The IIM therefore is still the most accurate approach.

We also perform calculations by considering two materials of great difference in modulus, e.g. $E_1/E_2 = 100$. The calculated SIFs are compared with those reported in the Ref. [55], as seen in Fig. 16. We can see the two computational results agree well.

4.3. A circular arc crack in an infinite bimaterial sample

As the last example, we consider a non-planar crack. A circular arc crack lying along the interface of a disk embedded in an infinite domain subjected to a biaxial extension σ is widely employed in literature [55,56]. As shown in Fig. 17(a), the length of the

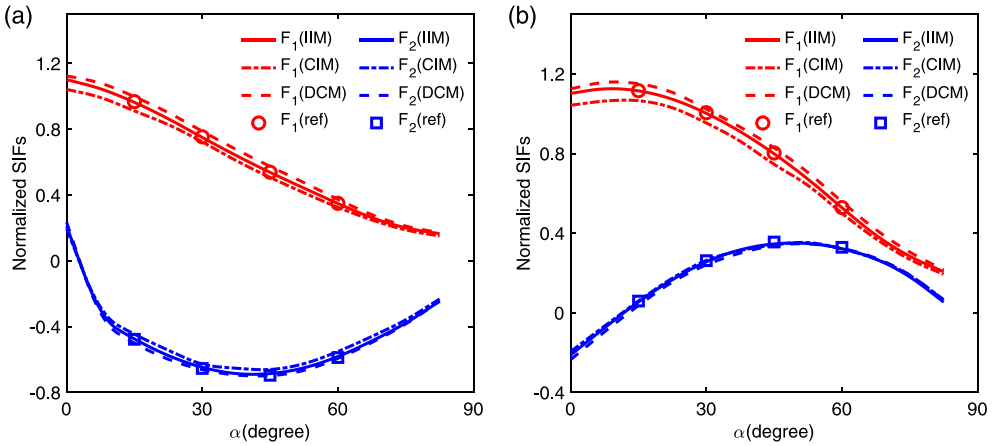

Fig. 16. Normalized SIFs at the (a) left and (b) right crack tip of the center crack problem with $E_1/E_2 = 100$.

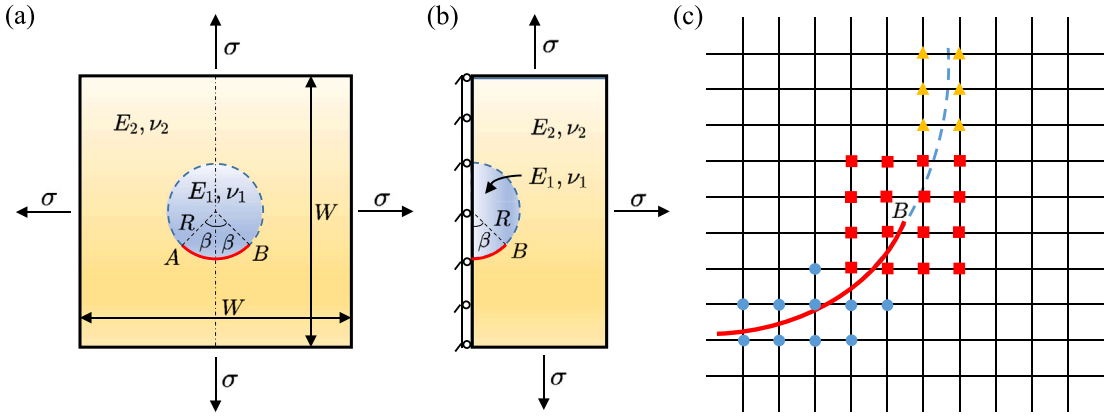

Fig. 17. A circular arc crack: (a) geometry and boundary conditions; (b) numerical model; and (c) enriching strategy.

square is $W = 20$ and the radius of the circle is $R = 1$. We here set $W = 20R$ to avoid the boundary effects. As shown in Fig. 17(b), we only model the right half of the sample due to the symmetry of the problem and introduce the symmetric boundary conditions. The half arc-angle β varies at $30°, 45°, 60°$ and $90°$. The Poisson ratios are identical as $\nu_1 = \nu_2 = 0.3$, but we study the ratio E_1/E_2 from 1 to 100. Fig. 17(c) shows the enriching scheme with the ramp functions.

4.3.1. *Validation of the X-FEM code for curved cracks*

We again validate our X-FEM code via comparisons with FEM. Fig. 18(a) shows the displacement along y-axis obtained by the ABAQUS by setting a singular element at the crack tip within the framework of FEM. Fig. 18(b) is the result for our code. We can see the distributions of the displacement are almost identical.

4.3.2. *Enrichment schemes*

We also first check the effects of enriching schemes. Four mesh sizes, e.g. $10\times20, 20\times40, 30\times60$, 40×80 and 50×100 elements, are employed. As mentioned above, we use the solution of the finest grid as reference. Fig. 19 plots the convergence curves for the case of $\beta = 90°$. The convergence rate of sch1 is 1.657 while that of sch2 is 1.126. Similar to the planar crack problems, sch1 is still more accurate than sch2 for the curve crack problems. Note that the non-planar crack is discretized by a set of straight line segments.

4.3.3. *Extraction of SIFs*

We first point out that only the IIM and DCM are employed to extract SIFs for the curve crack lying on the interface of bimaterials, abandoning the CIM since more efforts should be paid for the derivations and implementations, which is rarely reported in the literature. However, we can find reference SIFs for various angles as comparisons [56,57]. For the IIM, the extraction parameter is still set to $\rho = 3$, while for the DCM, we set $\Delta = 0.5h, N = 11$, $\rho = 0.3l_c/h$ with l_c representing the length of the discretized line segment for the crack.

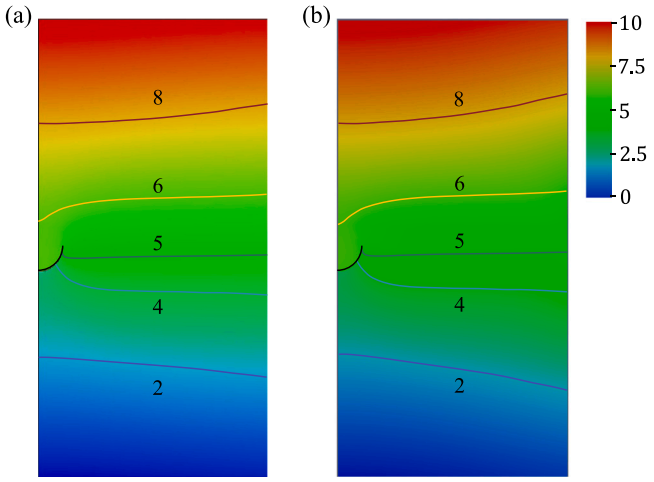

Fig. 18. Comparison of displacement fields along y direction for a circular arc crack problem (a) ABAQUS and (b) X-FEM.

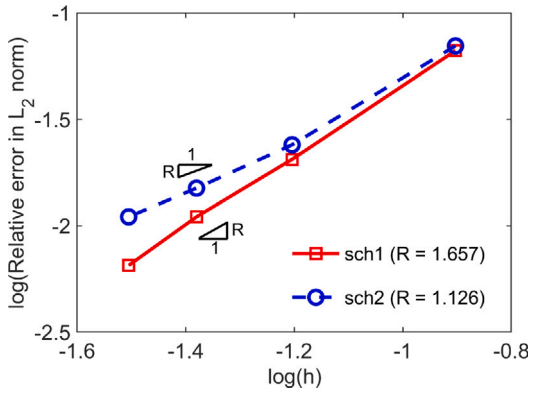

Fig. 19. Relative error in L_2 norm using different enrichment schemes.

Table 3
Normalized SIFs for the arc-shaped crack problem in homogeneous materials.

	β	30° (Error %)	45° (Error %)	60° (Error %)	90° (Error %)
Exact	F_1	0.6401	0.6776	0.6447	0.4714
	F_2	0.1715	0.2807	0.3722	0.4714
IIM	F_1	0.6437 (0.5655)	0.6862 (1.2741)	0.6550 (1.5913)	0.4810 (2.0335)
	F_2	0.1755 (2.3434)	0.2706 (3.5914)	0.3672 (1.3479)	0.4610 (2.2123)
DCM	F_1	0.6458 (0.8861)	0.6879 (1.5196)	0.6454 (0.1140)	0.4706 (0.1720)
	F_2	0.1765 (2.9015)	0.2885 (2.7752)	0.3823 (2.7257)	0.4721 (0.1589)

Similar to (47), we define two types of non-dimensional SIFs:

$$F_1 = \frac{K_{\mathrm{I}}}{\sigma\sqrt{\pi R}}, \quad F_2 = \frac{K_{\mathrm{II}}}{\sigma\sqrt{\pi R}}, \tag{48}$$

and

$$|K| = \frac{\sqrt{K_I^2 + K_{II}^2}}{\sigma\sqrt{\pi R}}. \tag{49}$$

For homogeneous materials, E_1 equals to E_2 and we use (48) to compare the computational results with the reference results [50,58,59], as shown in Table 3 and Fig. 20. We can see that both the IIM and the DCM can obtain acceptable SIFs for various β.

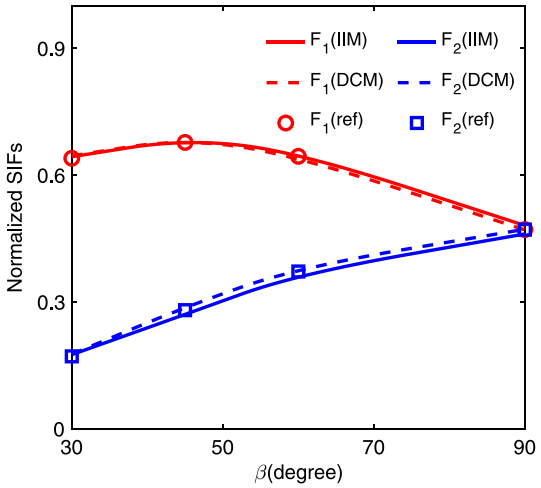

Fig. 20. Normalized SIFs for the arc-shaped crack problem in homogeneous materials.

Table 4
Normalized SIFs for the arc-shaped crack problem in inhomogeneous materials.

β	E_1/E_2	30° (Error %)	60° (Error %)	90° (Error %)
Ref	1	0.663	0.744	0.667
	5	0.876	1.068	1.029
	20	0.911	1.134	1.140
	100	0.918	1.149	1.171
IIM	1	0.6672 (0.6335)	0.7509 (0.9274)	0.6662 (0.1199)
	5	0.8605 (1.7695)	1.0891 (1.9747)	1.0389 (0.9592)
	20	0.9165 (0.6010)	1.1097 (2.1473)	1.1946 (4.7868)
	100	0.9278 (1.0649)	1.1097 (3.4212)	1.2157 (3.8173)
DCM	1	0.6695 (0.9804)	0.7502 (0.8330)	0.6667 (0.0500)
	5	0.8711 (0.5564)	1.0985 (2.8577)	1.0178 (1.0865)
	20	0.9300 (2.0899)	1.1607 (2.3536)	1.1860 (4.0377)
	100	0.9434 (2.7632)	1.1826 (2.9199)	1.2159 (3.8301)

For inhomogeneous materials, it is hardly to decompose the mixed patterns to modes I and II, and we therefore use (49) to measure the SIFs. We conduct simulations for different cases with $E_1/E_2 = 5, 20$ and 100, as well as $\beta = 30°, 60°$ and 90°. The results are summarized in Table 4. The SIFs are in good agreement with the reference solution [56] and the discrepancies between numerical solutions and the reference solutions can narrow within 5% for any case. However, we should point that the error increases with the ratio of elastic moduli, which is also observed in [42]. This may be caused by the fact that (13) will be inaccurate for large ratio of the moduli. We also compare the condition numbers and find that they increase with the ratio. Larger conditions numbers may introduce larger errors for the same convergence criterion of the solver of the linear system. The normalized SIFs $|K|$ vary with respect to β with different ratios of elastic moduli as shown in Fig. 21.

5. Conclusions

In this work, we performed a comprehensive exploration on existing numerical techniques developed for X-FEM to compute the SIFs of cracks lying on the interface of two dissimilar materials. Two different enriching schemes, with and without ramp functions, to describe the interface are investigated. Three routines to calculate the SIFs are explored, including the IIM, CIM, and DCM. To assure the robustness of conclusions, we further considered their applications to interface cracks of a variety of geometrical features, such as edge-crack, slated-crack, and circular-arc crack. We obtain the following conclusions.

1. The ramp functions can improve the solution in terms of strain energy, but do not significantly affect the condition numbers of the stiffness matrix and the SIFs.
2. Among three methods to extract SIFs, the IIM seems to be the most accurate one. The DCM can supply reasonable accuracy, conditioned on the right choice of the extraction parameter and the adoption of interpolation schemes.
3. The relative error of SIFs for curved crack increases with the discrepancies in elastic properties between the dissimilar materials, but falls within 5% in present exploration.

To conclude, we hope a reader interested in X-FEM to explore the SIFs of interface cracks may find it helpful in choosing the right enriching strategies and the extraction methods for SIFs.

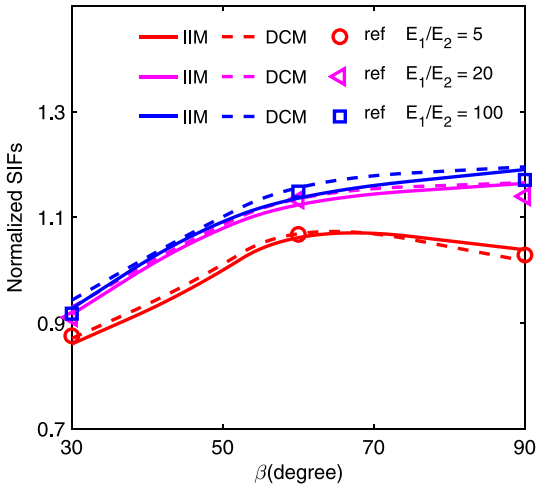

Fig. 21. Normalized SIFs for the arc-shaped crack problem in inhomogeneous materials.

CRediT authorship contribution statement

Min Ru: Writing – original draft, Investigation. **Chuanqi Liu:** Writing – review & editing, Supervision. **Yujie Wei:** Writing – review & editing, Supervision.

Declaration of competing interest

The authors declare the following financial interests/personal relationships which may be considered as potential competing interests: Chuanqi Liu reports financial support was provided by National Natural Science Foundation of China. Chuanqi Liu reports financial support was provided by Chinese Academy of Sciences.

Data availability

Data will be made available on request.

Acknowledgments

Y. Wei acknowledges support from the National Natural Science Foundation of China, China (NSFC) (No. 11988102, No. 11790291), and C. Liu thanks support from NSFC, China (No. 12172368) and the One Hundred Talents Program of Chinese Academy of Sciences (CAS), China.

Appendix. Complementary functions in the CIM

The complementary functions are given as follows [47].

$$\left(\widetilde{\sigma}_{11}\right)_j = \widetilde{M}_1 \left\{ c_1 \left[\widetilde{f}^{\mathrm{I}}_{11}\omega_j - \omega_j^{-1}\cos(2\theta - \Theta) \right] + c_2 \left[\widetilde{f}^{\mathrm{II}}_{11}\omega_j - \omega_j^{-1}\sin(2\theta - \Theta) \right] \right\}, \tag{A.1}$$

$$\left(\widetilde{\sigma}_{22}\right)_j = \widetilde{M}_1 \left\{ c_1 \left[\widetilde{f}^{\mathrm{I}}_{22}\omega_j + \omega_j^{-1}\cos(2\theta - \Theta) \right] + c_2 \left[\widetilde{f}^{\mathrm{II}}_{22}\omega_j + \omega_j^{-1}\sin(2\theta - \Theta) \right] \right\}, \tag{A.2}$$

$$\left(\widetilde{\sigma}_{12}\right)_j = \widetilde{M}_1 \left\{ c_1 \left[\widetilde{f}^{\mathrm{I}}_{12}\omega_j - \omega_j^{-1}\sin(2\theta - \Theta) \right] + c_2 \left[\widetilde{f}^{\mathrm{II}}_{12}\omega_j + \omega_j^{-1}\cos(2\theta - \Theta) \right] \right\}, \tag{A.3}$$

$$\left(\widetilde{u}_1\right)_j = \widetilde{M}_2 \left[c_1 \left(-\kappa_j\omega_j\widetilde{h}_{11} + \omega_j^{-1}\widetilde{h}_{12} + \omega_j\widehat{h}_{13} \right) + c_2 \left(\kappa_j\omega_j\widetilde{h}_{21} - \omega_j^{-1}\widetilde{h}_{22} + \omega_j\widetilde{h}_{23} \right) \right], \tag{A.4}$$

$$\left(\widetilde{u}_2\right)_j = \widetilde{M}_2 \left[c_1 \left(\kappa_j\omega_j\widetilde{h}_{21} - \omega_j^{-1}\widetilde{h}_{22} - \omega_j\widetilde{h}_{23} \right) + c_2 \left(\kappa_j\omega_j\widetilde{h}_{11} - \omega_j^{-1}\widetilde{h}_{12} + \omega_j\widetilde{h}_{13} \right) \right], \tag{A.5}$$

where

$$\Theta = \frac{1}{2}\theta + \varepsilon \ln r, \tag{A.6}$$

$$\omega_j = \begin{cases} e^{-\varepsilon(\pi-\theta)} & j=1 \\ e^{\varepsilon(\pi+\theta)} & j=2, \end{cases} \tag{A.7}$$

$$\widetilde{M}_1 = \frac{1}{2\sqrt{2\pi r^3}}, \tag{A.8}$$

$$\widetilde{M}_2 = \frac{1}{2G_j\sqrt{2\pi r}}, \tag{A.9}$$

$$\widetilde{f}_{11}^{\mathrm{I}} = 3\cos\theta\cos(2\theta+\Theta) + 2\varepsilon\sin\theta\cos(2\theta+\Theta), \tag{A.10}$$

$$\widetilde{f}_{11}^{\mathrm{II}} = -3\cos\theta\sin(2\theta+\Theta) - 2\varepsilon\sin\theta\sin(2\theta+\Theta), \tag{A.11}$$

$$\widetilde{f}_{22}^{\mathrm{I}} = \cos(\theta+\Theta) - 2\varepsilon\sin\theta\cos(2\theta+\Theta) + 3\sin\theta\sin(2\theta+\Theta), \tag{A.12}$$

$$\widetilde{f}_{22}^{\mathrm{II}} = -\sin(\theta+\Theta) + 2\varepsilon\sin\theta\sin(2\theta+\Theta) + 3\sin\theta\cos(2\theta+\Theta), \tag{A.13}$$

$$\widetilde{f}_{12}^{\mathrm{I}} = \sin(\theta+\Theta) + 2\varepsilon\sin\theta\sin(2\theta+\Theta) + 3\sin\theta\cos(2\theta+\Theta), \tag{A.14}$$

$$\widetilde{f}_{12}^{\mathrm{II}} = \cos(\theta+\Theta) + 2\varepsilon\sin\theta\cos(2\theta+\Theta) - 3\sin\theta\sin(2\theta+\Theta), \tag{A.15}$$

$$\widetilde{h}_{11} = \frac{(\cos\Theta - 2\varepsilon\sin\Theta)}{(1+4\varepsilon^2)}, \tag{A.16}$$

$$\widetilde{h}_{12} = \frac{[\cos(\theta-\Theta) + 2\varepsilon\sin(\theta-\Theta)]}{(1+4\varepsilon^2)}, \tag{A.17}$$

$$\widetilde{h}_{13} = \sin\theta\sin(\theta+\Theta), \tag{A.18}$$

$$\widetilde{h}_{21} = \frac{(\sin\Theta + 2\varepsilon\cos\Theta)}{(1+4\varepsilon^2)}, \tag{A.19}$$

$$\widetilde{h}_{22} = \frac{[-\sin(\theta-\Theta) + 2\varepsilon\cos(\theta-\Theta)]}{(1+4\varepsilon^2)}, \tag{A.20}$$

$$\widetilde{h}_{23} = \sin\theta\cos(\theta+\Theta). \tag{A.21}$$

Thus the particular complementary solution leading to the representation formula (31) for K_I results if the arbitrary constant c_1 and c_2 in above equations are chosen to be

$$c_1 = \frac{4G_1G_2}{G_2(\kappa_1+1) + G_1(\kappa_2+1)}, \tag{A.22}$$

$$c_2 = -\frac{8\varepsilon G_1G_2}{G_2(\kappa_1+1) + G_1(\kappa_2+1)}, \tag{A.23}$$

whereas (32) for K_{II} results from

$$c_1 = \frac{8\varepsilon G_1G_2}{G_2(\kappa_1+1) + G_1(\kappa_2+1)}, \tag{A.24}$$

$$c_2 = \frac{4G_1G_2}{G_2(\kappa_1+1) + G_1(\kappa_2+1)}. \tag{A.25}$$

References

[1] Barut A, Guven I, Madenci E. Analysis of singular stress fields at junctions of multiple dissimilar materials under mechanical and thermal loading. Int J Solids Struct 2001;38(50–51):9077–109.
[2] Chen L, Liu G, Zeng K, Zhang J. A novel variable power singular element in G space with strain smoothing for bi-material fracture analyses. Eng Anal Bound Elem 2011;35(12):1303–17.
[3] Saouma V, Schwemmer D. Numerical evaluation of the quarter-point crack tip element. Internat J Numer Methods Engrg 1984;20(9):1629–41.
[4] Banks-Sills L. Application of the finite element method to linear elastic fracture mechanics. 1991.
[5] Lim I, Johnston I, Choi S. Application of singular quadratic distorted isoparametric elements in linear fracture mechanics. Internat J Numer Methods Engrg 1993;36(14):2473–99.
[6] Belytschko T, Black T. Elastic crack growth in finite elements with minimal remeshing. Internat J Numer Methods Engrg 1999;45(5):601–20.
[7] Moës N, Dolbow J, Belytschko T. A finite element method for crack growth without remeshing. Internat J Numer Methods Engrg 1999;46(1):131–50.
[8] Daux C, Moës N, Dolbow J, Sukumar N, Belytschko T. Arbitrary branched and intersecting cracks with the extended finite element method. Internat J Numer Methods Engrg 2000;48(12):1741–60.
[9] Melenk J, Babuška I. The partition of unity finite element method: basic theory and applications. Comput Methods Appl Mech Engrg 1996;139(1–4):289–314.

[10] Huang R, Prevost J, Huang Z, Suo Z. Channel-cracking of thin films with the extended finite element method. Eng Fract Mech 2003;70(18):2513–26.
[11] Sukumar N, Huang Z, Prévost J, Suo Z. Partition of unity enrichment for bimaterial interface cracks. Internat J Numer Methods Engrg 2004;59(8):1075–102.
[12] Huynh D, Belytschko T. The extended finite element method for fracture in composite materials. Internat J Numer Methods Engrg 2009;77(2):214–39.
[13] Jung J, Jeong C, Taciroglu E. Identification of a scatterer embedded in elastic heterogeneous media using dynamic XFEM. Comput Methods Appl Mech Engrg 2013;259:50–63.
[14] Yu T, Bui T, Liu P, Zhang C, Hirose S. Interfacial dynamic impermeable cracks analysis in dissimilar piezoelectric materials under coupled electromechanical loading with the extended finite element method. Int J Solids Struct 2015;67:205–18.
[15] Dimitri R, Fantuzzi N, Li Y, Tornabene F. Numerical computation of the crack development and SIF in composite materials with XFEM and SFEM. Compos Struct 2017;160:468–90.
[16] Bouhala L, Shao Q, Koutsawa Y, Younes A, Núñez P, Makradi A, et al. An XFEM crack-tip enrichment for a crack terminating at a bi-material interface. Eng Fract Mech 2013;102:51–64.
[17] Liu X, Xiao Q, Karihaloo B. XFEM for direct evaluation of mixed mode SIFs in homogeneous and bi-materials. Internat J Numer Methods Engrg 2004;59(8):1103–18.
[18] Wang Y, Cerigato C, Waisman H, Benvenuti E. XFEM with high-order material-dependent enrichment functions for stress intensity factors calculation of interface cracks using Irwin's crack closure integral. Eng Fract Mech 2017;178:148–68.
[19] Ashari S, Mohammadi S. Delamination analysis of composites by new orthotropic bimaterial extended finite element method. Internat J Numer Methods Engrg 2011;86(13):1507–43.
[20] Hutchinson J, Suo Z. Mixed mode cracking in layered materials. Adv Appl Mech 1991;29:63–191.
[21] Zeng X, Wei Y. Crack deflection in brittle media with heterogeneous interfaces and its application in shale fracking. J Mech Phys Solids 2017;101:235–49.
[22] Liu Z, Wei Y. An analytical solution to the stress fields of kinked cracks. J Mech Phys Solids 2021;156:104619.
[23] Williams M. The stresses around a fault or crack in dissimilar media. Bull Seismol Soc Am 1959;49(2):199–204.
[24] Rice J, Sih G. Plane problems of cracks in dissimilar media. 1965.
[25] Toya M. A crack along the interface of a circular inclusion embedded in an infinite solid. J Mech Phys Solids 1974;22(5):325–48.
[26] Ryoji Y, Sang-Bong C. Efficient boundary element analysis of stress intensity factors for interface cracks in dissimilar materials. Eng Fract Mech 1989;34(1):179–88.
[27] Lan X, Ji S, Noda N, Cheng Y. Stress intensity factor solutions for several crack problems using the proportional crack opening displacements. Eng Fract Mech 2017;171:35–49.
[28] Chan S, Tuba I, Wilson W. On the finite element method in linear fracture mechanics. Eng Fract Mech 1970;2(1):1–17.
[29] Ingraffea A, Manu C. Stress-intensity factor computation in three dimensions with quarter-point elements. Internat J Numer Methods Engrg 1980;15(10):1427–45.
[30] Banks-Sills L, Sherman D. Comparison of methods for calculating stress intensity factors with quarter-point elements. Int J Fract 1986;32(2):127–40.
[31] Gupta P, Duarte C, Dhankhar A. Accuracy and robustness of stress intensity factor extraction methods for the generalized/eXtended Finite Element Method. Eng Fract Mech 2017;179:120–53.
[32] Mazurowski B, O'Hara P, Gupta P, Duarte C. A displacement correlation method for stress intensity factor extraction from 3D fractures in anisotropic materials. Eng Fract Mech 2021;258:108040.
[33] Mazurowski B, Sanchez-Rivadeneira A, Shauer N, Duarte C. High-order stable generalized/extended finite element approximations for accurate stress intensity factors. Eng Fract Mech 2021;241:107308.
[34] Yau J, Wang S. An analysis of interface cracks between dissimilar isotropic materials using conservation integrals in elasticity. Eng Fract Mech 1984;20(3):423–32.
[35] Miyazaki N, Ikeda T, Soda T, Munakata T. Stress intensity factor analysis of interface crack using boundary element method—application of contour-integral method. Eng Fract Mech 1993;45(5):599–610.
[36] Nagai M, Ikeda T, Miyazaki N. Stress intensity factor analysis of a three-dimensional interface crack between dissimilar anisotropic materials. Eng Fract Mech 2007;74(16):2481–97.
[37] Huang K, Guo L, Yu H, Jia P, Kitamura T. A domain-independent interaction integral method for evaluating the dynamic stress intensity factors of an interface crack in nonhomogeneous materials. Int J Solids Struct 2016;100:547–57.
[38] Rice J. A path independent integral and the approximate analysis of strain concentration by notches and cracks. 1968.
[39] Moran B, Shih C. Crack tip and associated domain integrals from momentum and energy balance. Eng Fract Mech 1987;27(6):615–42.
[40] Stern M, Becker E, Dunham R. A contour integral computation of mixed-mode stress intensity factors. Int J Fract 1976;12(3):359–68.
[41] Szabo B, Babuška I. Computation of the amplitude of stress singular terms for cracks and reentrant corners. In: Fracture mechanics: nineteenth symposium, ASTM STP. Vol. 969. 1988, p. 101–24.
[42] Wang Y, Waisman H. Material-dependent crack-tip enrichment functions in XFEM for modeling interfacial cracks in bimaterials. Internat J Numer Methods Engrg 2017;112(11):1495–518.
[43] Pereira J, Duarte C. Extraction of stress intensity factors from generalized finite element solutions. Eng Anal Bound Elem 2005;29(4):397–413.
[44] Pereira J, Duarte C. The contour integral method for loaded cracks. Commun Numer Methods Eng 2006;22(5):421–32.
[45] Garzon J, Duarte C, Pereira J. Extraction of stress intensity factors for the simulation of 3-D crack growth with the generalized finite element method. In: Key engineering materials. Vol. 560. Trans Tech Publ; 2013, p. 1–36.
[46] Hong C, Stern M. The computation of stress intensity factors in dissimilar materials. J Elasticity 1978;8(1):21–34.
[47] Yang X, Kuang Z. Contour integral method for stress intensity factors of interface crack. Int J Fract 1996;78(3):299–313.
[48] Deng X. General crack-tip fields for stationary and steadily growing interface cracks in anisotropic bimaterials. 1993.
[49] Moës N, Cloirec M, Cartraud P, Remacle J. A computational approach to handle complex microstructure geometries. Comput Methods Appl Mech Engrg 2003;192(28–30):3163–77.
[50] Wang Y, Waisman H, Harari I. Direct evaluation of stress intensity factors for curved cracks using Irwin's integral and XFEM with high-order enrichment functions. Internat J Numer Methods Engrg 2017;112(7):629–54.
[51] Smelser R, Gurtin M. On the J-integral for bi-material bodies. Int J Fract 1977;13(3):382–4.
[52] Yau J, Wang S, Corten H. A mixed-mode crack analysis of isotropic solids using conservation laws of elasticity. 1980.
[53] Natarajan S, Song C. Representation of singular fields without asymptotic enrichment in the extended finite element method. Internat J Numer Methods Engrg 2013;96(13):813–41.
[54] Arndt D, Bangerth W, Blais B, Clevenger T, Fehling M, Grayver A, et al. The deal. II library, version 9.2. J Numer Math 2020;28(3):131–46.
[55] Gu Y, Zhang C. Novel special crack-tip elements for interface crack analysis by an efficient boundary element method. Eng Fract Mech 2020;239:107302.
[56] Tan C, Gao Y. Treatment of bimaterial interface crack problems using the boundary element method. Eng Fract Mech 1990;36(6):919–32.
[57] Perlman A, Sih G. Elastostatic problems of curvilinear cracks in bonded dissimilar materials. Internat J Engrg Sci 1967;5(11):845–67.
[58] Sih G, Paris P, Erdogan F. Crack-tip, stress-intensity factors for plane extension and plate bending problems. 1962.
[59] Huang R, Sukumar N, Prévost J. Modeling quasi-static crack growth with the extended finite element method Part II: Numerical applications. Int J Solids Struct 2003;40(26):7539–52.